Preliminary research on dual-energy X-ray phase-contrast imaging *

Hua-Jie Han(韩华杰)[1,2] Sheng-Hao Wang(王圣浩)[1] Kun Gao(高昆)[1;1)] Zhi-Li Wang(王志立)[1]
Can Zhang(张灿)[1] Meng Yang(杨萌)[1] Kai Zhang(张凯)[3;2)] Pei-Ping Zhu(朱佩平)[3]

[1] National Synchrotron Radiation Laboratory, University of Science and Technology of China, Hefei 230027, China
[2] School of Engineering Science, University of Science and Technology of China, Hefei 230027, China
[3] Institute of High Energy Physics, Chinese Academy of Sciences, Beijing 100049, China

Abstract: Dual-energy X-ray absorptiometry (DEXA) has been widely applied to measure the bone mineral density (BMD) and soft-tissue composition of the human body. However, the use of DEXA is greatly limited for low-Z materials such as soft tissues due to their weak absorption, while X-ray phase-contrast imaging (XPCI) shows significantly improved contrast in comparison with the conventional standard absorption-based X-ray imaging for soft tissues. In this paper, we propose a novel X-ray phase-contrast method to measure the area density of low-Z materials, including a single-energy method and a dual-energy method. The single-energy method is for the area density calculation of one low-Z material, while the dual-energy method aims to calculate the area densities of two low-Z materials simultaneously. Comparing the experimental and simulation results with the theoretical ones, the new method proves to have the potential to replace DEXA in area density measurement. The new method sets the prerequisites for a future precise and low-dose area density calculation method for low-Z materials.

Keywords: X-ray imaging, dual-energy, phase-contrast, area density

PACS: 87.59.-e, 42.30.Rx, 06.30.Dr **DOI:** 10.1088/1674-1137/40/4/048201

1 Introduction

The idea of dual-energy X-ray absorptiometry can be traced back to the 1970s, when the method of differentiating low-Z materials from high-Z materials with a dual-energy scan was first proposed by Hounsfield [1]. Following his work, researchers including Zatz and Alvarez et al. [2–4] reported the advantages of the dual-energy method in material differentiation. In 1976, R. A. Rutherford utilized a dual-energy scan to determine the effective atomic number and electron density of materials, and applied it to human tissue imaging [5]. Recently, dual-energy absorptiometry has found increasingly wide applications in the fields of clinical diagnosis, public security, etc [6–12]. As an application, dual-energy X-ray absorptiometry is the "gold standard" in bone mineral density (BMD) measurement, and it can also be used to obtain the percentage fat in soft tissue, fat mass and lean tissue mass [6–8].

However, low-Z materials, such as soft tissues, show weak absorption of X-rays. Besides, different soft tissues show similar characteristics in X-ray absorption [13]. Therefore, conventional absorption-based dual-energy CT has an inherent defect in material differentiation for weak absorption materials [14]. While X-ray phase-contrast imaging offers a dramatically higher contrast for weak absorbers as reported in the past few decades [15–17], the reason lies in the refraction coefficient exceeding the absorption coefficient by at least three orders of magnitude. Moreover, the refraction coefficients of different soft tissues vary greatly [15].

In this paper, an innovative dual-energy phase-contrast method is proposed, which is able to remarkably promote the quality of identification and differentiation of weakly absorbing materials, and meanwhile decrease the radiation dose. Firstly, we derive the equations for area density calculation, including single-energy method and dual-energy method. Secondly, based on the experimental results and a numerical simulation, we demonstrate the feasibility of the methods. Finally, we discuss the experimental data and potential applications of the new dual-energy phase-contrast imaging method.

Received 19 May 2015, Revised 25 November 2015

∗ Supported by Major State Basic Research Development Program (2012CB825800), Science Fund for Creative Research Groups (11321503) and National Natural Science Foundation of China (11179004, 10979055, 11205189, 11205157)

1) E-mail: gaokun@ustc.edu.cn

2) E-mail: zhangk@ihep.ac.cn

2 Theory

When a beam of X-rays penetrates an object, the variation of the intensity is given by

$$I = I_0 \mathrm{e}^{-\mu t}, \tag{1}$$

where I_0 is the intensity of the incident X-ray, I represents the intensity of the emergent X-ray, t is the transmission length, and μ is the linear attenuation coefficient. Generally, Eq. (1) is written as

$$I = I_0 \mathrm{e}^{-(\mu/\rho)\rho t}, \tag{2}$$

where ρ is the density of the substance, and μ/ρ is known as the mass attenuation coefficient, which is determined by the characteristics of the substance, and ρt is the area density of the substance, denoted by M. The area density is thus given by

$$M = -\frac{\ln(I/I_0)}{\mu/\rho}. \tag{3}$$

The precise measurement of BMD is crucial for the diagnosis of osteoporosis [18], and dual-energy X-ray absorptiometry actually measures the area density of bones [6], which is primary work for further information extraction. Area density is usually expressed in g/cm^2, and is used to describe the bone mass per unit of projected area, or the average mass per pixel. In order to diminish the error introduced by the soft tissues, the dual-energy method is proposed in the measurement [18]. For each projection, two images at different levels of energy are obtained with the dual-energy method. For the human body, the penetration of dual-energy X-rays can be expressed by

$$I_L = I_{0L} \exp\left[-(\mu/\rho)_{LS} M_S - (\mu/\rho)_{LB} M_B\right], \tag{4}$$

$$I_H = I_{0H} \exp\left[-(\mu/\rho)_{HS} M_S - (\mu/\rho)_{HB} M_B\right], \tag{5}$$

where subscripts L and H represent low and high energy, respectively; and subscripts B and S represent bone and soft tissue, respectively. Supposing that $U_{LS}=(\mu/\rho)_{LS}$, $U_{HS} = (\mu/\rho)_{HS}$, $U_{LB} = (\mu/\rho)_{LB}$, $U_{HB} = (\mu/\rho)_{HB}$, $R_S = U_{LS}/U_{HS}$, $R_B = U_{LB}/U_{HB}$, the area density of the soft tissue and the bone can be obtained from Eq. (4) and (5) as follows:

$$M_S = \frac{R_B \ln(I_H/I_{0H}) - \ln(I_L/I_{0L})}{U_{LS} - U_{HS} R_B}, \tag{6}$$

$$M_B = \frac{R_S \ln(I_H/I_{0H}) - \ln(I_L/I_{0L})}{U_{LB} - U_{HB} R_S}. \tag{7}$$

Accordingly, we can make a derivation from these formulas to calculate the area densities with dual-energy refraction data. The phase shift of X-rays when passing through an object is

$$\Phi = -k \int \delta \mathrm{d}t, \tag{8}$$

where $k = 2\pi/\lambda$ is the wave vector, δ is the phase factor and t is the transmission length. If the phase object is homogeneous, namely, the phase factor δ is evenly distributed, Eq. (7) can be rewritten as

$$\Phi = -k\delta t. \tag{9}$$

Likewise, we define the mass phase factor as δ/ρ. Since we know that the area density $M = \rho t$, Eq. (8) is further transformed to

$$\Phi = -k(\delta/\rho)M, \tag{10}$$

if we use cylindrical samples which are even along the length direction for theory deduction. Consequently, the phase shift Φ is simply a function of the radius direction (we denote it as the x direction), and the relationship between phase shift Φ and refraction angle α is correspondingly given by

$$\Phi = k \int \alpha(x) \mathrm{d}x. \tag{11}$$

Combining with the definition and assumptions as stated before, the area density function of the refraction angle is given by

$$M = -\frac{\left[\int \alpha(x) \mathrm{d}x\right]}{\delta/\rho}. \tag{12}$$

Similarly, the penetration of dual-energy X-rays through the human body can be described by

$$\Phi_L = -k(\delta/\rho)_{SL} M_S - k(\delta/\rho)_{BL} M_B, \tag{13}$$

$$\Phi_H = -k(\delta/\rho)_{SH} M_S - k(\delta/\rho)_{BH} M_B. \tag{14}$$

Supposing that $\Delta_{SL} = (\delta/\rho)_{SL}$, $\Delta_{SH} = (\delta/\rho)_{SH}$, $\Delta_{BL} = (\delta/\rho)_{BL}$, $\Delta_{BH} = (\delta/\rho)_{BH}$, $Z_S = \dfrac{\Delta_{SH}}{\Delta_{SL}}$, $Z_B = \dfrac{\Delta_{BH}}{\Delta_{BL}}$, then the area density of the soft tissue and the bone eventually become

$$M_B = \frac{\Phi_L Z_S - \Phi_H}{k\Delta_{BL}(Z_B - Z_S)}, \tag{15}$$

$$M_S = \frac{\Phi_L Z_B - \Phi_H}{k\Delta_{SL}(Z_S - Z_B)}. \tag{16}$$

3 Materials and methods

3.1 Experimental setup and working principles

For the experimental setup, a Talbot-Lau interferometer was used in combination with a tungsten rotating anode X-ray tube and a CCD detector constructed at the Institute of Multidisciplinary Research for Advanced Materials at Tohoku University, Japan, as illustrated by Fig. 1.

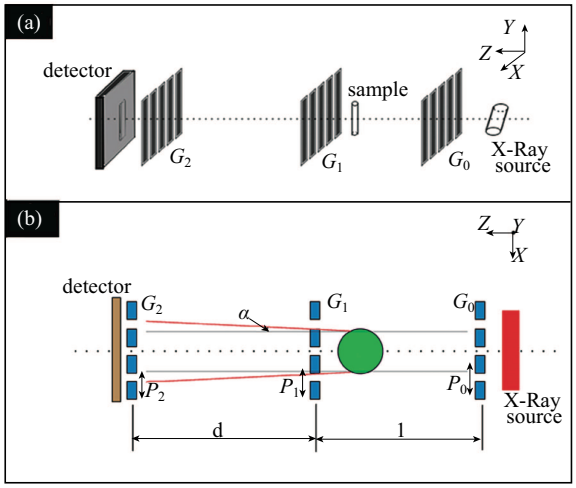

Fig. 1. (color online) Layout of hard-X-ray Talbot-Lau interferometer. (a) Schematic of Talbot-Lau interferometer. (b) Working principle of Talbot-Lau interferometer.

The working current of the X-ray tube is 45 mA, and the source grating G_0 (period $P_0 = 22.7$ μm, gold line height 70 μm, size 20mm×20 mm) is made of gold, about 80 mm downstream of the X-ray tube. The phase grating G_1 (period $P_1 = 4.36$ μm, gold line height 2.43 μm, size 50mm×50 mm) is situated 106.9 mm(l) downstream of the source grating. The phase grating is designed to generate a $\pi/2$ phase shift at a photon energy of 27 keV. The samples are positioned upstream of the phase grating at a distance of about 50 mm. The distance between the analyzer grating G_2 (period $P_2 = 5.4$ μm, gold line height 65 μm, size 50mm×50 mm) and the phase grating G_1 is 25.6 mm(d). The detector, a scintillator CCD camera with an effective receiving size of 68.4mm × 68.4 mm and pixel size of 18μm × 18 μm, is placed downstream of the analyzer grating G_2.

It is necessary to emphasize that the parameters of the optical elements are precisely designed and their relative positions are well optimized so as to obtain images of high quality. The working principles are desribed in Ref. [19]. The refraction angle α in the direction of axis x can be quantified by

$$\alpha = \frac{\lambda}{2\pi}\frac{\partial \Phi(x,y)}{\partial x}, \tag{17}$$

where x and y are the coordinates of the plane perpendicular to the optical axis, λ is the wavelength of the incident X-ray and $\Phi(x,y)$ represents the phase shift of the wavefront.

3.2 Data acquisition

Three phase objects were used for quantitative measurement and evaluation: one polymethyl methacrylate (PMMA) rod of 5 mm in diameter and two polyoxymethylene (POM) rods of 5 mm and 10 mm in diameter respectively. The three cylinders were all 100 mm in height. During the experimental operation, all of them were oriented parallel to the grating lines. A 5-step phase stepping scan was used in the experiment. First, the accelerating voltage of the tube was set at 35 kV, and the samples placed at the optical axis. Then the samples were removed and background images at 35 kV obtained. Thereafter, the accelerating voltage was ramped up to 45 kV, with the procedure of data acquisition exactly the same.

3.3 Information extraction

The absorption signal and the refraction signal are retrieved by the following equations [20]:

$$A(m,n) = \ln\left[\frac{\sum_{k=1}^{N} I_k^s(m,n)}{\sum_{k=1}^{N} I_k^b(m,n)}\right], \tag{18}$$

$$\alpha(m,n) = \frac{P_2}{2\pi d}\times \arg\left[\frac{\sum_{k=1}^{N} I_k^s(m,n)\times \exp\left(2\pi \mathrm{i}\frac{k}{N}\right)}{\sum_{k=1}^{N} I_k^b(m,n)\times \exp\left(2\pi \mathrm{i}\frac{k}{N}\right)}\right], \tag{19}$$

where (m,n) denotes the pixel position of the CCD sensor, N is the number of the steps, subscript k represents that the data is obtained at the k^{th} step, and superscripts s and b denote that the samples are added and removed, respectively. P_2 is the period of the analyzer grating G_2, and d is the distance between G_1 and G_2.

4 Results

4.1 Information extraction

Figure 2 shows the absorption images and refraction images obtained from Eqs. (18) and (19).

Specifically, Fig. 2(a) shows the absorption image at the accelerating voltage of 35 kV, while Fig. 2(b) is its counterpart of the refraction image; Fig. 2(c) shows the absorption image at the accelerating voltage of 45 kV, and Fig. 2(d) is its counterpart of the refraction image.

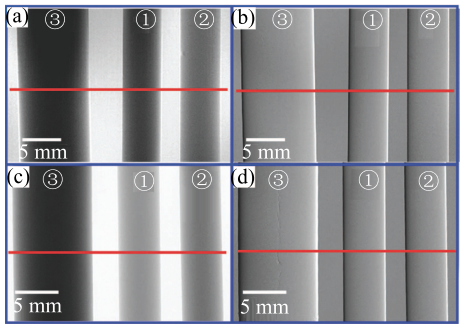

Fig. 2. (color online) Absorption and refraction images of the samples. (a) Absorption image at the tube voltage of 35 kV. (b) Refraction image at the tube voltage of 35 kV. (c) Absorption image at the tube voltage of 45 kV. (d) Refraction image at the tube voltage of 45 kV. The rods are also numbered, where ① is for the PMMA rod, ② is for the POM rod with the diameter of 5 mm and ③ is for the POM rod with the diameter of 10 mm. All images are windowed for optimized appearance with a linear gray scale.

4.2 Single-energy calculation

First, we calculate the area density of the samples with the single-energy phase-contrast method. A cross section of the samples is selected for the calculation, denoted in Fig. 2 by the red lines. The results are plotted in Fig. 3, and the parameters necessary for the calculation are listed in Table 1.

The black and red curves in Fig. 3 plot the area densities calculated based on the conventional absorption method and the proposed phase-contrast method, respectively, in comparison with the theoretical prediction highlighted by the blue curve. In order to quantify the calculation errors, the centric positions of the samples are chosen for comparison, denoted in Fig. 3 by the yellow dashed lines. The values and mathematical errors are listed in Table 2. In the table, superscripts Theo and Cal represent theoretical values and calculated values, respectively, and E_L and E_H represent low energy (tube voltage 35 kV) and high energy (tube voltage 45 kV), respectively.

4.3 Dual-energy calculation

This subsection investigates the feasibility of the dual-energy phase-contrast method described by Eqs. (15) and (16), aiming to compute the area densities of two materials simultaneously. A numerical simulation is carried out on a contrast phantom whose cross section is shown in Fig. 4.

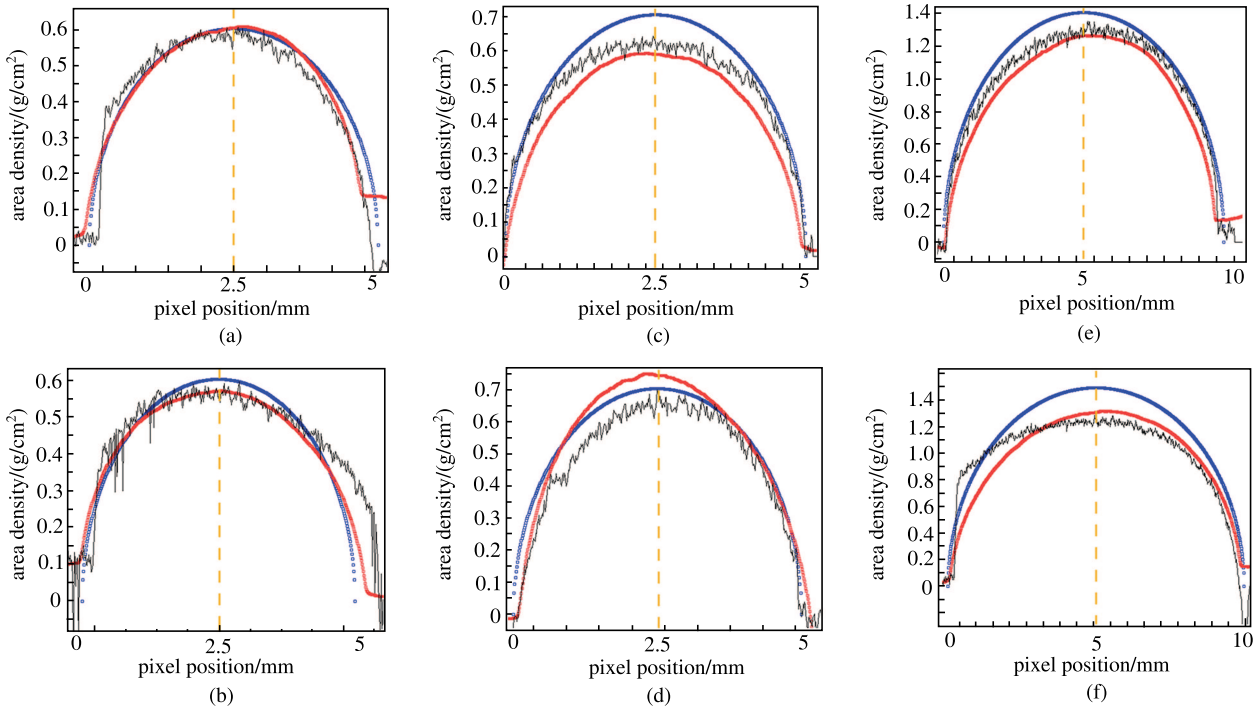

Fig. 3. (color online) Results for the area density calculation along the cross section with the absorption method, refraction method and theoretical results, shown by black lines, red lines and blue lines respectively. (a) Results of sample ① at the tube voltage of 35 kV. (b) Results of sample ① at the tube voltage of 45 kV. (c) Results of sample ② at the tube voltage of 35 kV. (d) Results of sample ② at the tube voltage of 45 kV. (e) Results of sample ③ at the tube voltage of 35 kV. (f) Results of sample ③ at the tube voltage of 45 kV.

Table 1. The absorption and refraction factor at different energies, and the densities of the samples [21].

tube voltage(mean energy)	PMMA		POM	
	absorption $\beta(\times10^{-10})$	refraction $\delta(\times10^{-7})$	absorption$\beta(\times10^{-10})$	refraction$\delta(\times10^{-7})$
35 kV(25 keV)	1.53018681	4.26404711	2.03051909	5.0097696
45 kV(27.5 keV)	1.22495458	3.52414105	1.60430406	4.1531670
$\rho/(\mathrm{g/cm^3})$	1.19		1.42	

Table 2. Area density comparison between the calculation values and the theoretical values at centric positions of the samples.

samples	$M^{\mathrm{Theo}}/(\mathrm{g/cm^2})$	absorption method				refraction method			
		E_L		E_H		E_L		E_H	
		$M^{\mathrm{Cal}}/(\mathrm{g/cm^2})$	%Error	$M^{\mathrm{Cal}}/(\mathrm{g/cm^2})$	%error	$M^{\mathrm{Cal}}/(\mathrm{g/cm^2})$	%error	$M^{\mathrm{Cal}}/(\mathrm{g/cm^2})$	%error
①PMMA	0.595	0.58	−2.52	0.57	−4.20	0.60	0.84	0.56	−5.88
②POM	0.71	0.62	−12.6	0.69	−2.82	0.57	−19.7	0.74	4.23
③POM	1.42	1.3	−8.45	1.19	−16.1	1.25	−11.9	1.32	−7.04

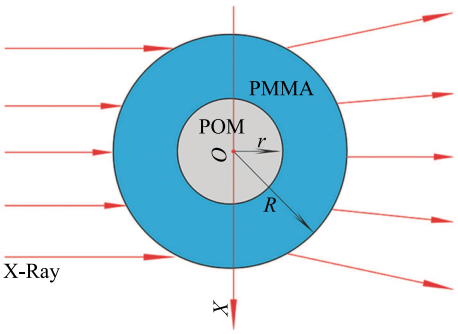

Fig. 4. (color online) The cross section of the contrast phantom used for the simulation.

As the illustration shows, the phantom consists of a core cylinder made of POM, closely encircled by a cylindrical chamber made of PMMA ($r=5$ cm, $R=10$ cm). As before, we still set the tube voltage at 35 kV and 45 kV. Thus, the refraction angle of the X-ray $\theta(x)$ can be described as [20]

$$\theta(x)=\begin{cases} -\dfrac{2\delta_{\mathrm{PMMA}}x}{\sqrt{R^2-x^2}}, r\leqslant|x|<R \\ \dfrac{2\delta_{\mathrm{PMMA}}x}{\sqrt{r^2-x^2}}-\dfrac{2\delta_{\mathrm{PMMA}}x}{\sqrt{R^2-x^2}}-\dfrac{2\delta_{\mathrm{POM}}x}{\sqrt{r^2-x^2}}, |x|<r \end{cases} \tag{20}$$

where we define the radius direction as axis x and the center of the cross section as the origin, as shown in Fig. 4. To simplify the simulation, we define

$$\Theta=\int\theta(x)\mathrm{d}x. \tag{21}$$

Figure 5 is a schematic representation of the simulation process. Fig. 5(a) shows the variation of the refraction angle according to the pixel position at the tube voltage of 35 kV and Fig. 5(b) is the integration thereof. Figure 5(c) and 5(d) are the corresponding simulation results at the tube voltage of 45 kV.

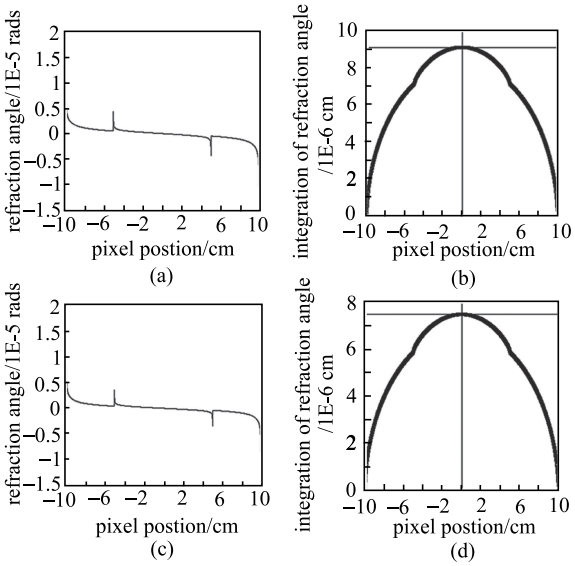

Fig. 5. Sketch of the simulation process. (a) Simulation of refraction angle at tube voltage of 35 kV. (b) Simulation of the integration of refraction angle at tube voltage of 35 kV. (c) Simulation of refraction angle at tube voltage of 45 kV. (d) Simulation of the integration of refraction angle at tube voltage of 45 kV.

Again the centric position of the phantom is selected for comparison with the theoretical values. As Fig. 5 shows, $\Theta_L = 9.08765\times10^{-6}$ and $\Theta_H = 7.50131\times10^{-6}$. Based on the data in Table 1, we can deduce that $\Delta_{SL}=(\delta/\rho)_{SL}=3.58323287\times10^{-7}$, $\Delta_{SH}=(\delta/\rho)_{SH}=2.96146307\times10^{-7}$, $\Delta_{BL}=(\delta/\rho)_{BL}=3.60390141\times10^{-7}$,

$\Delta_{BH}=(\delta/\rho)_{BH} = 2.97178169\times10^{-7}$, $Z_S = \dfrac{\Delta_{SH}}{\Delta_{SL}} = 0.82647798$, $Z_B=\dfrac{\Delta_{BH}}{\Delta_{BL}}=0.82460127$, consequently,

$$M_{\rm POM}=\frac{\Theta_L Z_S-\Theta_H}{\Delta_{BL}(Z_B-Z_S)}=13.94\ ({\rm g/cm^2}),$$

$$M_{\rm PMMA}=\frac{\Theta_L Z_B-\Theta_H}{\Delta_{SL}(Z_S-Z_B)}=11.335\ ({\rm g/cm^2}).$$

According to our assumption, however, the theoretical values ought to be

$$M_{\rm POM}=\rho_{\rm POM}\times D_{\rm POM}=14.2\ ({\rm g/cm^2}),$$

$$M_{\rm PMMA}=\rho_{\rm PMMA}\times D_{\rm PMMA}=11.9\ ({\rm g/cm^2}),$$

where $D_{\rm POM}$ and $D_{\rm PMMA}$ represent the transmission length of the core cylinder and the chamber cylinder at the centric position respectively. Naturally, the simulation errors are calculated as follows.

$$\Delta_{\rm POM}=\frac{M^{\rm Cal}_{\rm POM}-M^{\rm Theo}_{\rm POM}}{M^{\rm Theo}_{\rm POM}}\times100\%=-1.83\%,$$

$$\Delta_{\rm PMMA}=\frac{M^{\rm Cal}_{\rm PMMA}-M^{\rm Theo}_{\rm PMMA}}{M^{\rm Theo}_{\rm PMMA}}\times100\%=-4.75\%,$$

where superscript Cal represents simulation values and superscript Theo represents the theoretical values.

Similarly, the area densities of the contrast phantom can be calculated with the absorption-based method described by Eqs. (6) and (7) at the centric position. Using the data listed in Table 1, we can work out that $U_{LB}=(\mu/\rho)_{LB}=0.362244$, $U_{HS}=(\mu/\rho)_{HS}=0.286846$, $U_{LS}=(\mu/\rho)_{LS}=0.325747$, $U_{HB}=(\mu/\rho)_{HB}=0.314829$, $R_B=U_{LB}/U_{HB}=1.150609$, $R_S=U_{LS}/U_{HS}=1.135617$, and consequently,

$$M_S=\frac{R_B\ln(I_H/I_{0H})-\ln(I_L/I_{0L})}{U_{LS}-U_{HS}R_B}=11.899928({\rm g/cm^2}),$$

$$M_B=\frac{R_S\ln(I_H/I_{0H})-\ln(I_L/I_{0L})}{U_{LB}-U_{HB}R_S}=14.200008({\rm g/cm^2}).$$

Likewise, the simulation errors are

$$\Delta_{\rm POM}=\frac{M^{\rm Cal}_{\rm POM}-M^{\rm Theo}_{\rm POM}}{M^{\rm Theo}_{\rm POM}}=5.634\times10^{-7},$$

$$\Delta_{\rm PMMA}=\frac{M^{\rm Cal}_{\rm PMMA}-M^{\rm Theo}_{\rm PMMA}}{M^{\rm Theo}_{\rm PMMA}}=-6.0504\times10^{-6}.$$

5 Discussion

Figure 3 shows the calculation results with the absorption method and the novel phase-contrast method while Table 2 quantifies the corresponding calculation errors, which both prove the validity of the proposed method (calculation error is generally <5%). Moreover, the errors can result from: (1) the parameter gauge of the apparatus, the optical elements and the samples; (2) the absorption and refraction of air. Furthermore, it is worth noticing that there is a lot of noise in the absorption data, but the refraction data follow a relatively smooth curve. The distinction between the calculation processes is able to explain the divergence. In the refraction calculation method, an integration is contained, which is actually a filtering operation, but the absorption method is based on the original images, making the absorption method inferior to the refraction method in terms of noise reduction. Nevertheless, calculation errors can also be introduced by the integration, and further work should be done to quantify the errors.

Additionally, the phase-contrast method suffers greater error in comparison with the absorption-based method, as shown in Fig. 3. Due to the difference in computational method between the two methods, the errors can be explained. For the absorption-based method, the area density is calculated with Eq. (3), where term $ln(I/I_0)$ is read directly from the detector. For the phase-contrast method, however, the calculation equation is Eq. (12), where only the refraction angle $\alpha(x)$ is directly read, resulting in an integration process being used. The integration can cause errors in the refraction of air; as mentioned before, the error introduced by the refraction of air should be estimated, and the integration actually has a significant amplification effect on the errors. Although a refraction correction is introduced before calculation, eliminating the error utterly is impossible. Error is also introduced in the jump of the refraction angle. Theoretically, the distribution of the refraction angle follows the equation $\theta(x)=-\dfrac{2\delta x}{\sqrt{R^2-x^2}}$. Obviously, at the edge of the cylinders ($x=R$), $\theta(x)$ tends to infinity, so the calculation formula can approximately calculate the area density.

As stated before, the new dual-energy method is devoted to the accurate calculation of low-Z materials, so two low-Z materials close to each other in effective atomic number ($Z_{\rm PMMA}=6.47$, $Z_{\rm POM}=6.95$) are employed in the numerical simulation. It is striking that the simulation errors of the absorption-based method are near zero, which is consistent with the theoretical expectations. However, the simulation results obtained by the phase-contrast method have a certain error (simulation errors are -4.75% and -1.83%, respectively). Likewise, the error sources can be analyzed as: (1) theoretically, the refraction angle at the cylinder edge approaches infinity, so the simulation involves an approximation; (2) the integration to determine the phase shift involves errors.

Though the simulation error of the absorption-based method is much less than the phase-contrast method, it is improper to make any conclusion as to which method is better because of the large gap between numerical simulation and practical application. The accuracy of the two methods will undoubtedly be lower in application, but the new method has a much better contrast for soft tissues and there is still enough room for improvement of the computational method. In brief, the new method is superior in imaging quality, but the absorption-based method performs better in imaging processing, and much future effort is required to make a detailed analysis and comparison between them.

X-ray phase-contrast imaging possesses evidently better contrast compared to the conventional absorption-based imaging for low-Z materials, while they perform similarly for high-Z materials. So the dual-energy phase-contrast method has certain advantages over the dual-energy absorption method, which can briefly be summarized as follows. Firstly, the new method lowers the radiation dose. With the novel dual-energy phase-contrast method, we can utilize X-ray sources with lower power and lower photon energy to obtain desirable images and calculation accuracy. Meanwhile, the radiation dose is reduced, which is critical if we aim to extend its utilization to clinical application. With current DEXA devices, the radiation dose of a complete checkup can be kept down to 100 μSv, while the photon energy used in the dual-energy phase-contrast method is only one third or half of conventional DEXA devices. Therefore, theoretically, the radiation dose can be cut to half of the DEXA method at least. Secondly, the calculation accuracy for bones as well as soft tissues can be improved. In bone density measurement, soft tissue density is also measured, and the measurement accuracy directly affects that of the bones. With the dual-energy phase-contrast method, soft tissue density can be measured with improved accuracy, which thus improves the bone density measurement as well. Thirdly, the use of contrast agents in certain operations can be reduced or eliminated. In existing dual-energy subtraction digital radiography, contrast agents are necessary because of the similarity of soft tissues (e.g. blood vessels and their surrounding tissues). The dual-energy phase-contrast method has an inherent merit in distinction of similar low-Z materials, so contrast agent is no longer needed and the operating procedure is simplified.

Although the new method has many advantages over the existing one, two major issues call for further intensive analysis. First, the tube voltage. For typical X-ray wavelengths employed in medical imaging, the refraction angles of soft tissues are usually smaller than 10 μrad. Naturally, improving the measurement sensitivity is essential, and increasing the tube voltage is an option to do this. However, higher energy can lead to lower differential phase contrast, and as a result, the selected photon energy of current X-ray phase-contrast imaging devices is always below 30 keV. With too low a photon energy, however, the penetration of X-ray declines, which impairs the imaging quality. The photon energies should be below and close to 30 keV. Meanwhile, the two selected energies should ensure that the differentiation of two tissues can be detected and calculated. Therefore, with required effective photon energy of 25 keV and 27.5 keV, the tube voltage is set at 35 kV and 45 kV, respectively. The experimental results also support the energy discussion before. Second, experimental materials. For a precise simulation and calculation of the human body with the new method to compare with DEXA, the experimental materials should be as similar to human tissue as possible. In current DEXA experiments, aluminum and PMMA are generally used to mimic bone and soft tissue, respectively, because they have similar optical properties with the X-ray we use. For this reason, it is convincing to simulate soft tissues with PMMA, but POM is inappropriate to simulate the bone. However, constrained by the experimental condition, it is hard to implement further experiments at present, and as a result, the current experiment data and analysis are merely able to demonstrate the validity of equation (15) and (16) in principle. In our future work, we plan to evaluate the practicability and accuracy of the new method in operation. Finally, the phase-contrast imaging method we employed is based on a Talbot-Lau interferometer, and it is generally optimized for a certain photon energy. As a result, the alteration of the tube voltage decreases the image quality. Hence we hope to develop a flexible dual-energy phase-contrast imaging method in the future.

6 Conclusion

In this paper, a novel phase-contrast method for area density calculation is presented, including single-energy method and dual-energy method. Experimental results from the refraction images and a numerical simulation demonstrate that the new method is applicable to area density measurement. Further extension of the work should include assessing the error with experiments on biological samples, quantifying the radiation dose, optimizing the dual X-ray energies and developing a flexible dual-energy phase-contrast imaging system. Moreover, another research endeavor is to apply dual-energy phase-contrast subtraction digital radiography in cardiovascular disease or inchoate cancer diagnosis, which may revolutionize these fields.

The authors would like to extend our sincere thanks to Fei-Fei Chen at the National University of Singapore, who checked through the paper with patience and gave

instructive suggestions. The authors also acknowledge financial funding support from the Japan-Asia Youth Exchange program in Science (SAKURA Exchange Program in Science) administered by the Japan Science and Technology Agency.

References

1 G. N. Hounsfield, Br. J. Radiol, **46**(552): 1016-1022 (1973)
2 R. E. Alvarez and A. Macovski, Phys. Med. Biol, **21**(5): 733(1976)
3 L. M. Zatz, Radiology, **119**(3): 683-688(1976)
4 A. Macovski, R. Alvarez, J. H. Chan et al, Comput. Biol. Med, **6**(4): 325-336(1976)
5 R. A. Rutherford, B. R. Pullan, and I. Isherwood, Neuroradiology, **11**(1): 15-21(1976)
6 R. B.Mazess, H. S. Barden, J. P.Bisek et al, Am. J. Clin. Nutr, **51**(6): 1106-1112(1990)
7 O. L. Svendsen, J. Haarbo, C. Hassager et al, Am. J. Clin. Nutr, **57**(5): 608-608(1993)
8 P. J. Ryan, in *Seminars in Nuclear Medicine*, Vol.27, edited by W. B. Saunders (1997), p. 291-305
9 G. Di Chiro, R. A. Brooks, M. Robert et al, Radiology, **131**(2): 521-523(1979)
10 L. J. Zhang, S. Y. Wu, C. S. Poon et al. J. Comput. Assist. Tomogr, **34**(6): 816-824(2010)
11 Macdonald, R. D. Richard, In *Photonics West 2001-Electronic Imaging*, (International Society for Optics and Photonics, 2001), p. 31-41
12 Z. R. Ying, R. Naidu, and C. R. Crawford, J. X-Ray Sci. Technol, **14**(4): 235-256(2006)
13 A. Momose, T. Takeda, Y. Itai et al, Nature Med, **2**(4): 473-475(1996)
14 C. Kottler, V. Revol, R. Kaufmann et al, J. Appl. Phys, **108**(11): 114906(2010)
15 A. Momose, Jpn. J. Appl. Phys, **44**(9R): 6355-6367(2005)
16 C. David, B. Nohammer, H. H. Solak et al, Appl. Phys. Lett, **81**(17): 3287-3289(2002)
17 S. Wilkins, T. Gureyev, D. Gao et al, Nature, **384**(6607): 335-338(1996)
18 S. J. Ostlere and R. H. Gold, Clin. Orthop. Relat. Res, **271**: 149-163(1991)
19 F. Pfeiffer, T. Weitkamp, O. Bunk et al, Nature Phys, **2**(4): 258-261(2006)
20 S. H. Wang, P. O. Margie, A. Momose et al, Chin. Phys. B, **6**(6): 673-678(2015)
21 http://henke.lbl.gov/optical_constants/getdb2.html, retrieved 25th April 2015